Supporting Information

Behind the transduction mechanism of a nanostructured functional material for environmental CO_2 monitoring

A. Rossi[a*], E. Ghedini[b,c], M. Signoretto[c], A. Gaiardo[d], M. Ferroni[e,f], M. Ardit[g], G. Vola[h], R. Tassinari[a], A. Pedrielli[d], L. Vanzetti[d], V. Guidi[a], and B. Fabbri[a]

S1. Results and Discussion

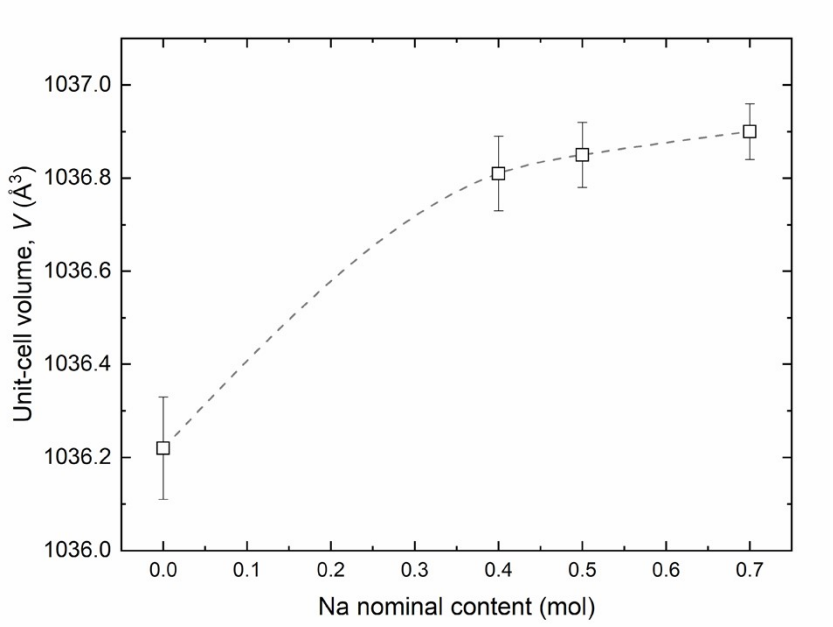

Fig. S1 Unit-cell volume of In_2O_3 samples as a function of nominal sodium content.

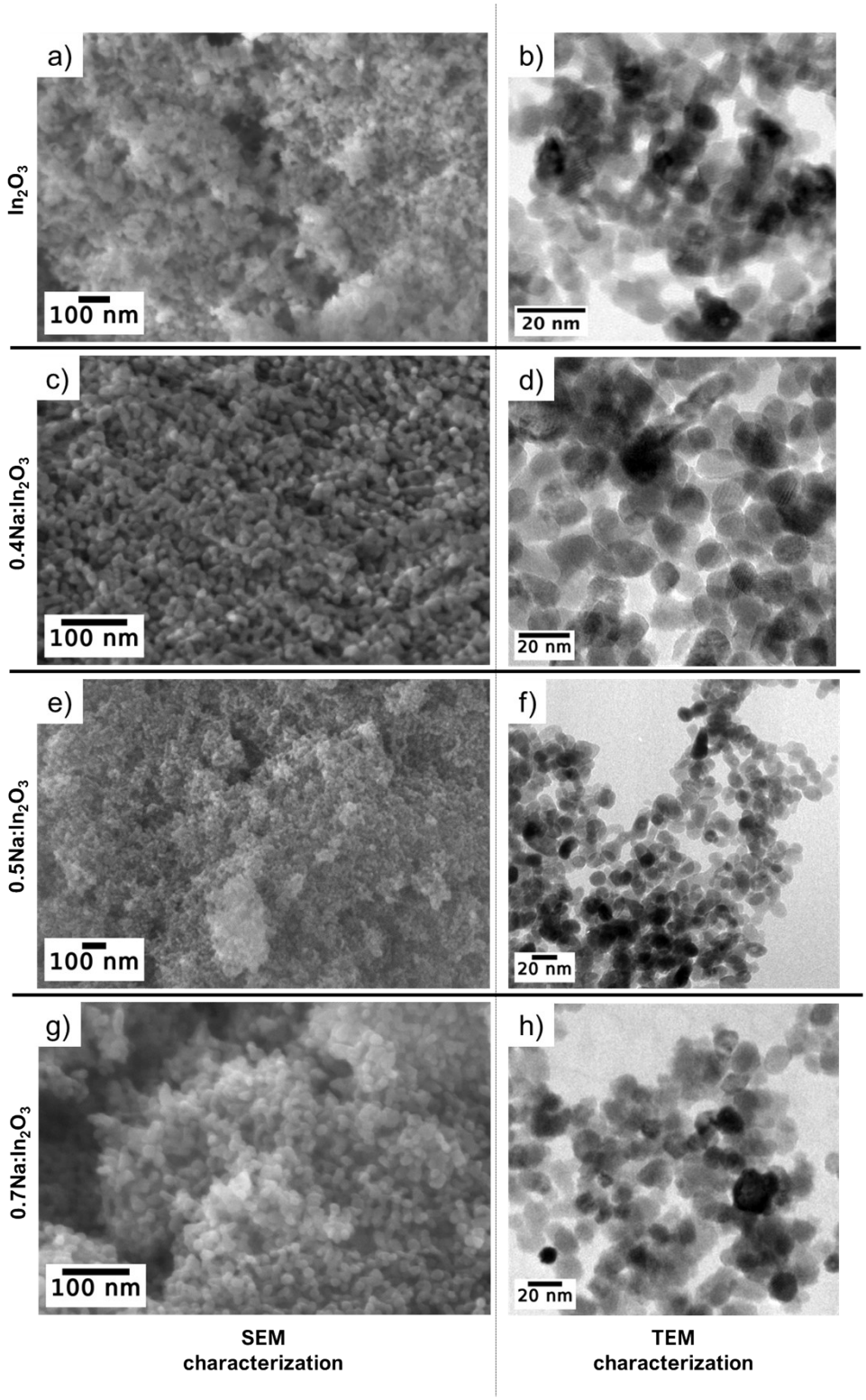

Fig. S2 SEM and TEM images, respectively, of (a, b) pristine In_2O_3, (c, d) 0.4Na:In_2O_3, (e, f) 0.5Na:In_2O_3, and (g, h) 0.7Na:In_2O_3 powders.

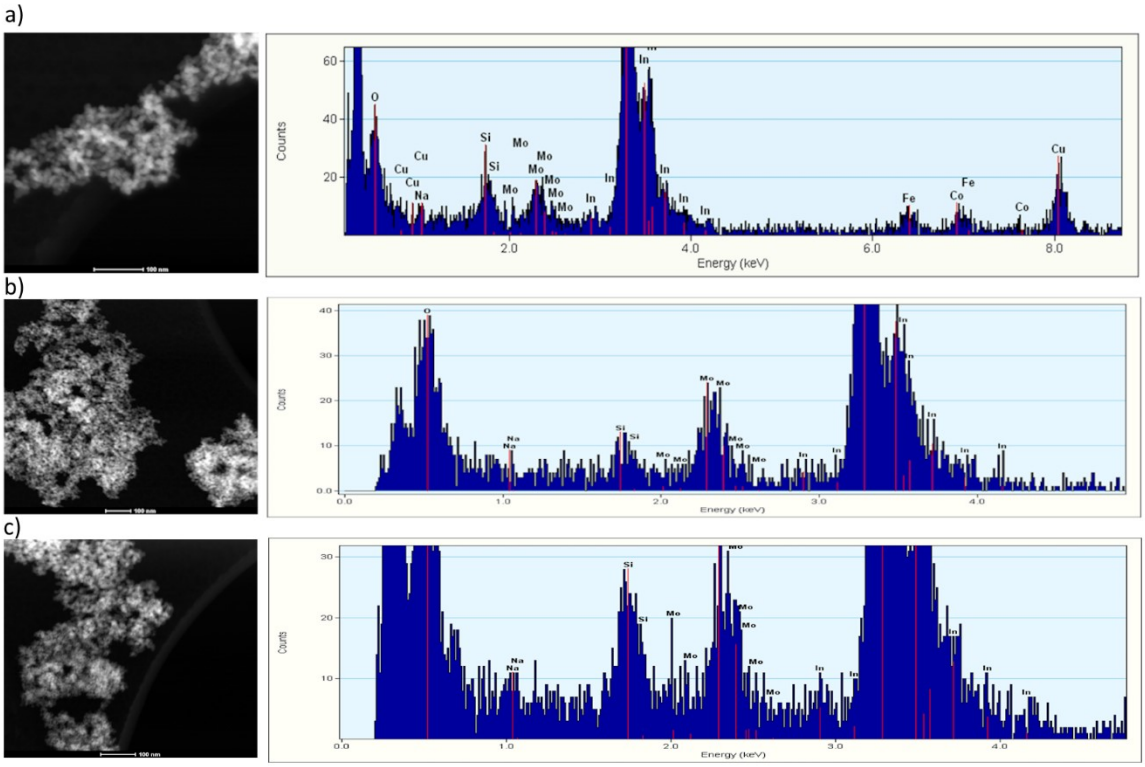

Fig. S3 STEM-EDX images of (a) 0.4Na:In_2O_3, (b) 0.5Na:In_2O_3, and (c) 0.7Na:In_2O_3. The Si, Cu, and Mo elements are present owing to the use of the sample support grid.

Table S1. Analytical results for the determination of sodium content in doped-samples by ICP-MS.

Element	**0.4Na:In_2O_3**	**0.5Na:In_2O_3**	**0.7Na:In_2O_3**
^{23}Na	17677 ppm	26609 ppm	36121 ppm

Table S2. Elemental composition [at%] and In 3d binding energies of the In_2O_3 and Na-doped In_2O_3 powders. Data obtained from **Fig. 3.4**.

Sample	**In $3d_{3/2}$ [eV]**	**In $3d_{5/2}$ [eV]**	**In [% at]**	**Na [% at]**	**O [% at]**	**C [% at]**
In_2O_3	451.6	444.1	38.70	0.000	51.10	10.20
0.4Na:In_2O_3	451.3	443.7	34.20	8.400	50.00	7.500
0.5Na:In_2O_3	451.4	443.8	33.00	6.700	48.50	11.80
0.7Na:In_2O_3	451.3	443.7	30.50	6.400	46.30	6.400

Table S3. Binding energies and relative quantitative analysis of the deconvolution O 1s peaks for doped samples. Data obtained from **Fig. S4**.

Sample	**O lattice (In – O – In)**		**H_2O – OH**		**HO – In**		**H_2O**	
	Binding Energy [eV]	**% peaks vs. O_{tot} [area]**	**Binding Energy [eV]**	**% peaks vs. O_{tot} [area]**	**Binding Energy [eV]**	**% peaks vs. O_{tot} [area]**	**Binding Energy [eV]**	**% peaks vs. O_{tot} [area]**
0.4Na:In_2O_3	529.4	54.0	530.4	22.0	531.4	20.0	532.6	4.00
0.5Na:In_2O_3	529.2	59.0	530.2	15.0	531.2	22.0	532.4	3.00
0.7Na:In_2O_3	529.6	59.0	530.2	14.0	531.2	23.0	532.4	4.00

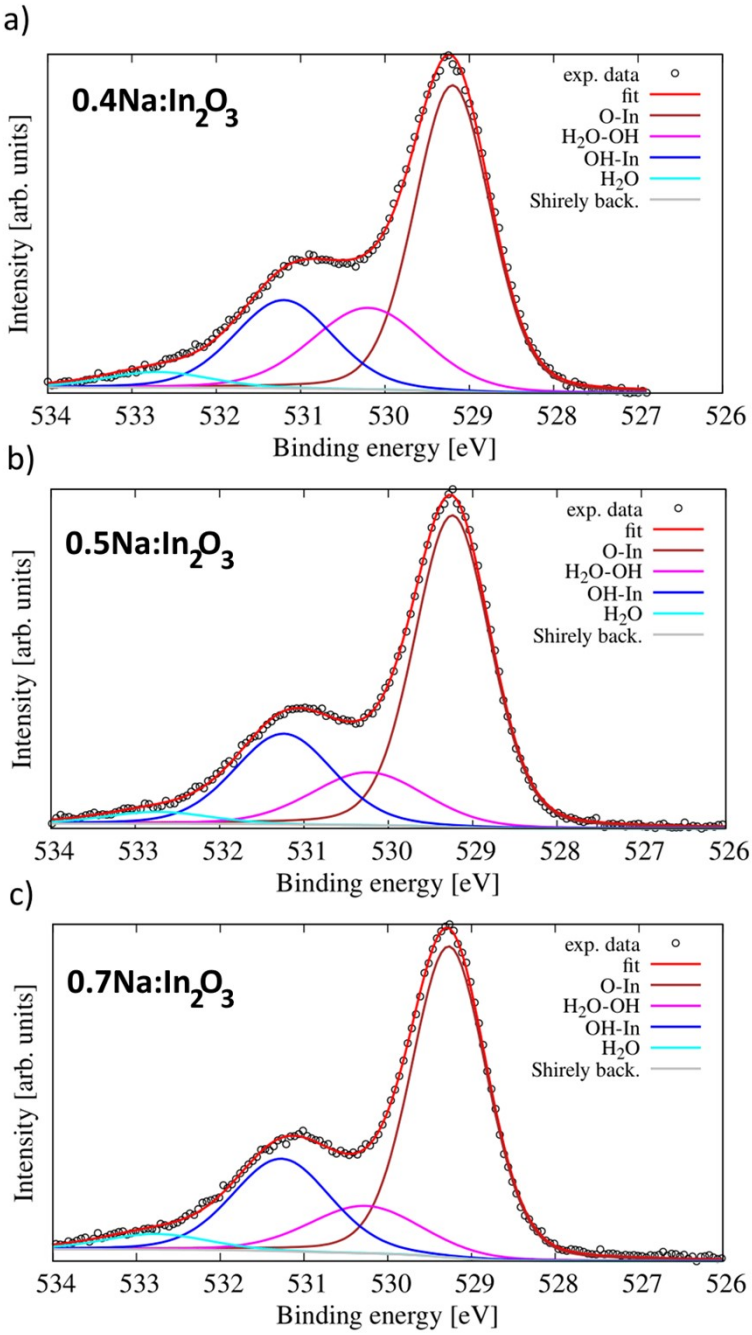

Fig. S4 High-resolution XPS spectra of O 1s using Shirely background, of (a) 0.4Na:In_2O_3, (b) 0.5Na:In_2O_3, and (c) 0.7Na:In_2O_3 powders.

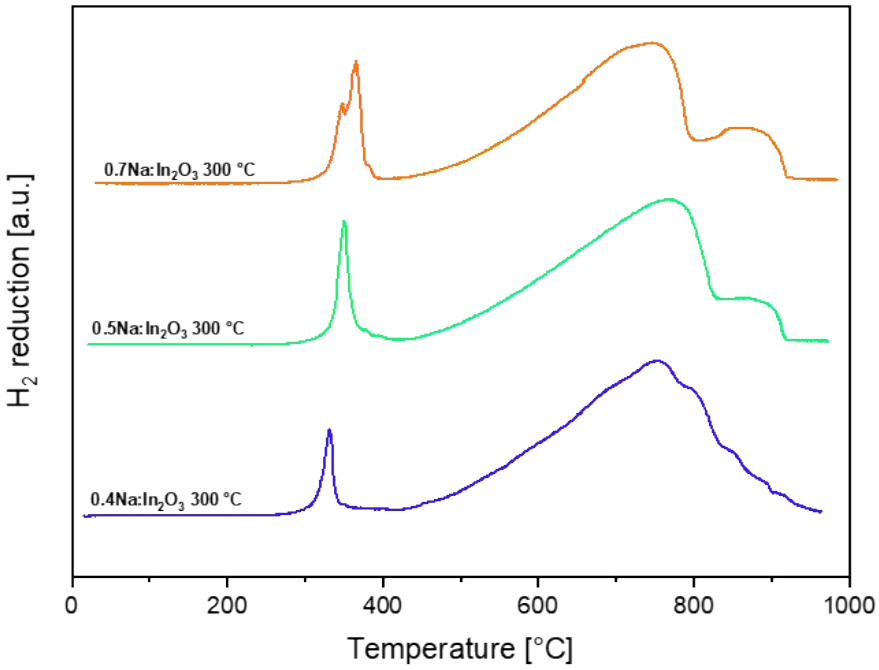

Fig. S5 TPR measurements with H_2. The samples were treated at 300 °C.

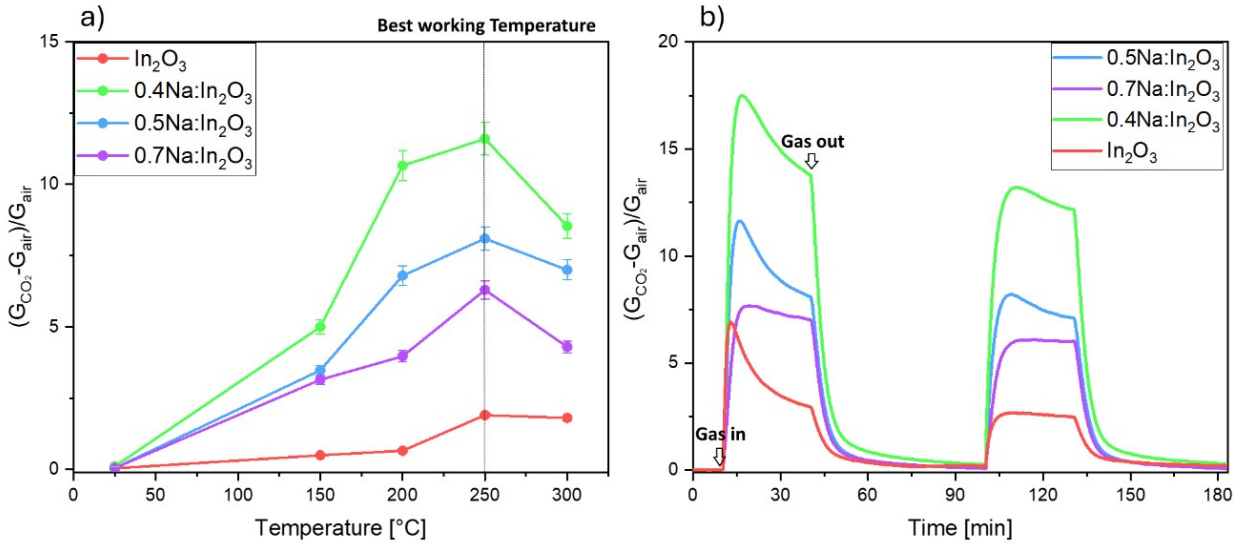

Fig. S6 (a) Response to 1000 ppm of CO_2 under different operating temperatures. (b) Dynamic response of the sensors at the best working temperature of 250 °C vs. 1000 ppm of CO_2. The error bars correspond to 5% of the instrumental error.

Table S4. Calibration parameters of the allometric function used to fit the sensors response in **Fig. 5a**. Uncertainties and estimated values are not rounded but left as they were provided by the spreadsheet. The coefficient of determination R^2 expresses the goodness of the fit.

Sensor	***a***	***b***	***R^2***
In_2O_3	0.345±0.051	0.254±0.019	0.98
0.4Na:In_2O_3	3.19±0.253	0.179±0.010	0.99
0.5Na:In_2O_3	2.28±0.181	0.183±0.010	0.99
0.7Na:In_2O_3	2.19±0.202	0.149±0.012	0.97

Table S5. Summary of the key sensor characteristics, including material properties (nominal Na amount, and actual Na content verified by ICP-MS, and structure), spectroscopic results (DRIFTS species observed), and electrical performance at the optimal working temperature of 250 °C (conductance in dry and wet conditions (20 RH%), sensor response vs 1000 ppm of analyte, and response/recovery times).

Sensor Label	*Na nominal*	*Actual Na content [ppm]*	*Crystalline structure*	*DRIFT species in dry air*	*Conductance in dry air [nS]*	*Conductance in wet conditions [nS]*	*Response*	*Response time [min]*	*Recovery time [min]*
In_2O_3	/	/	Cubic	- OH groups (3700-3200 cm^{-1}) - CO_2 (2366 and 2338 cm^{-1})	172	979	1.60	3	>20
0.4Na: In_2O_3	0.4 M	17677	Cubic	- OH groups (3700-3200 cm^{-1}) - CO_2 (2366 and 2338 cm^{-1}) - CO_3^{2-} (1600-1200 cm^{-1}) - In-O (1000-800 cm^{-1})	350	1070	13	3	9
0.5Na: In_2O_3	0.5 M	26609	Cubic	- OH groups (3700-3200 cm^{-1}) - CO_2 (2366 and 2338 cm^{-1}) - CO_3^{2-} (1600-1200 cm^{-1}) - In-O (1000-800 cm^{-1})	441	2002	9	5	6
0.7Na: In_2O_3	0.7 M	36121	Cubic	- OH groups (3700-3200 cm^{-1}) - CO_2 (2366 and 2338 cm^{-1}) - CO_3^{2-} (1600-1200 cm^{-1}) - In-O (1000-800 cm^{-1})	452	1772	8.5	11	12

An investigation on pure and doped powders was carried out because under *in-situ* DRIFT, exhibited high resolution. In particular, DRIFT spectra were acquired on both pure and doped powders at their best operating temperature, under dry and humid environments (16% RH). Significant differences were observed when comparing these results to the spectra obtained on the films. While previous film-based spectra did not show carbonate formation on the pristine sensor, the new acquisition on the powders revealed that carbonate species were present on the surface of the pristine sample in the 1500-1200 cm^{-1} region, confirming the activation of the surface toward CO_2. All materials displayed the presence of hydroxyl (-OH) groups, attributed to the physisorption of H_2O molecules. The absence of CO_2 physisorption on the pristine powder was also confirmed by these *in-situ* spectra.

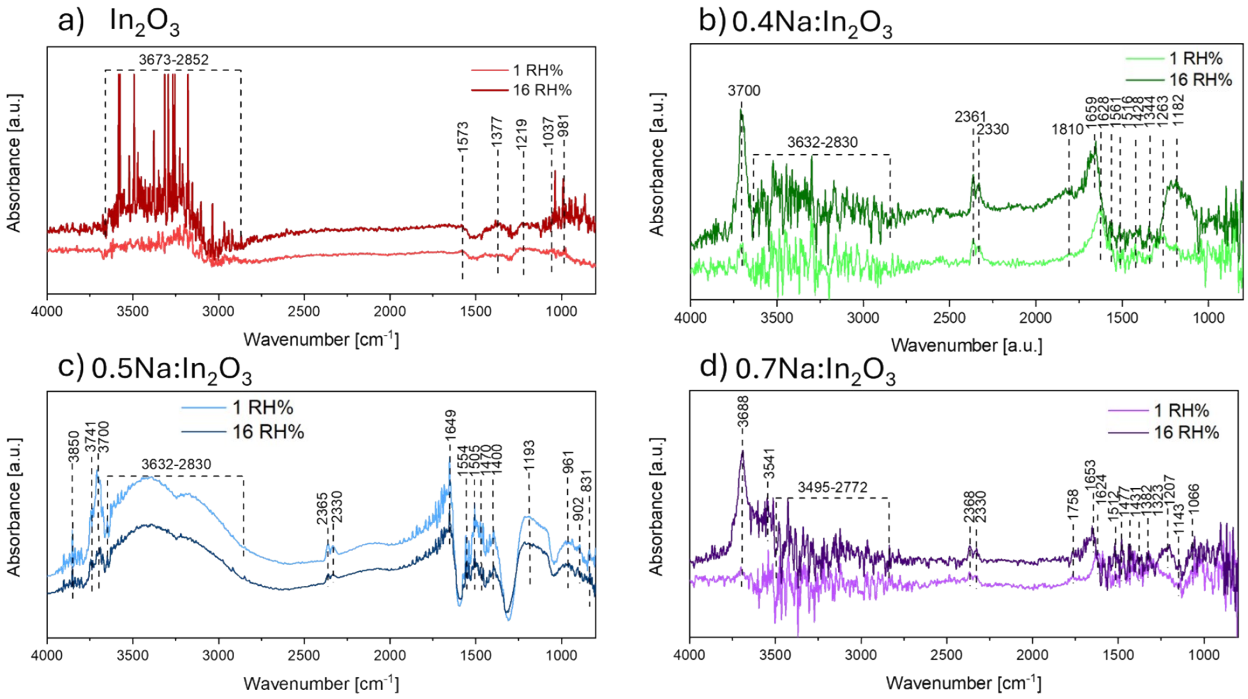

Fig. S7. Comparative *in-situ* DRIFT spectra of pure (a) In_2O_3 and sodium-doped indium oxide powders: (b) 0.4Na:In_2O_3, (c) 0.5Na:In_2O_3, and (d) 0.7Na:In_2O_3. These spectra were obtained in the presence of 1000 ppm CO_2, under both dry and wet conditions.

S2. Experimental Section

In this paragraph all the specifications of the instruments used in this work are reported.

XRPD analysis. X-Ray Powder Diffraction (XRPD) analyses were performed at room temperature using a Bruker D8 Advance Da Vinci diffractometer operating in Bragg-Brentano geometry and equipped with a LynxEye XE silicon strip detector (detector angular range: 2.585° 2θ) set to discriminate Cu $K\alpha_{1,2}$ radiation. *Rietveld refinement strategy*. Qualitative phase analysis of the collected patterns was carried out using the Bruker AXS EVA software (v.5). XRPD patterns were modelled using the fundamental-parameter Rietveld approach (TOPAS v.5.0, Bruker). Instrumental parameters (*e.g.*, goniometer radius, slit sizes, geometrical parameters of the X-ray tube, etc.) were used to calculate the instrumental contribution to the peak profiles. Specimen-related crystallite size and microstrain information were determined using the "integral breadth" algorithm from the observed profiles. The instrumental zero-error was fixed at the value determined using the NIST Si 640e standard. Together with a specimen-displacement correction and a nine-terms Chebyshev polynomial to model the background, the Rietveld refinement included the unit-cell parameters, crystallite size, and microstrain of the cubic In_2O_3 phase, starting from the structural model (fractional atomic coordinates and atomic displacement parameters, ADPs) reported by Marezio (1966).

***SEM-EDX characterization*.** The morphology and the chemical composition of nanostructured materials were investigated by a Zeiss LEO 1530 FEG microscope, equipped with an Oxford Inst. INCA 250 30 mm^2 SSD EDX spectrometer.

TEM and HR-TEM analyses. For TEM analyses, the powders were dispersed in isopropanol alcohol and sonicated. The solutions were dropping casting over a molybdenum or copper grid and dried on a heating plate. The measurements were performed by using a Philips TECNAI F20 ST TEM operating at 200 kV. The instrument was equipped with a EDAX SUTW EDX spectrometer and Fischione Inst. High-Angle Annular Dark-Field STEM imaging detector. TEM images were acquired in phase contrast mode and Selected Area Electron Diffraction (SAED). STEM images were recorded using a High Angle Annular Dark Field (HAADF) detector: in this imaging mode the intensity I is proportional to Z1.7t, where Z is the mean atomic number and t is the thickness of the specimen.

ICP-MS measurements. The Na concentrations in samples were determined using a Thermo Scientific iCAP TQ spectrometer. The powder samples were prepared by dissolving them in HNO3 (Suprapur®, Merck). After evaporation on a hotplate, the residue was taken up in Milli-Q water (I grade, 18,2 MΩ/cm at 25 °C) and transferred to a 100 mL volumetric flask. The flask was then filled to the mark with Milli-Q water. Before starting the measurements, the instrument had undergone routine conditioning and optimisation procedure. In order to control and correct signal fluctuations, an internal standard solution (^{6}Li and ^{103}Rh) was added online to the sample and standard calibration solution streams. The blank was also measured, and intensity was subtracted from that of samples.

XPS spectra. XPS analyses obtained during this work were performed using Kratos AXIS UltraDLD instrument (Kratos Analytical, Manchester, UK) equipped with a hemispherical analyser and a monochromatic Al Kα (1486.6 eV) X-ray source, in spectroscopy mode. The analyses were performed with a take-off angle between the analyser axis and the normal to the sample surface of 0°. For the

measurements, the powders were attached to the sample holder using double-sided carbon tape. For each sample, the survey and the high-resolution scans of the In 3d, O 1s and Na 1s core levels were collected. In particular, a Shirley background was employed to fit the O 1s peaks, using the Pseudo Voigt with coefficient of the Lorentzian 0.25 and Gaussian 0.75. XPS quantification was performed applying the instrument sensitivity factors to the high-resolution spectra. Charge compensation was achieved using a flood gun and all core levels were referenced to the C-C/C-H component in C 1s at 285.0 eV. All XPS data were analysed using the software described in Speranza and Canteri [ref].

BET measurements. Gas porosity and specific surface area of nanoparticles were investigated using a Micromeritics TriStar II Plus automated gas sorptometer, with a nominal resolution of > 0.01 m^2/g. The running program of N_2 adsorption-desorption isotherm consisted of 88 points of relative pressure, from 0.03 (p/p_0) up to 1.0 (p/p_0) and back, being the pressure of the adsorptive in equilibrium with the adsorbate and p0 the saturation vapour pressure of the adsorptive. The specific surface area was determined according to Brunauer-Emmett-Teller Specific Surface Area (BET-SSA) theory [ref]. Pore volume and pore-size distribution (PSD) were determined according to Adsorption/Desorption Barrett-Joyner-Halenda (BJH) method and to non-local density functional theory (DFT), respectively.